This is the preprint of the contribution published as:

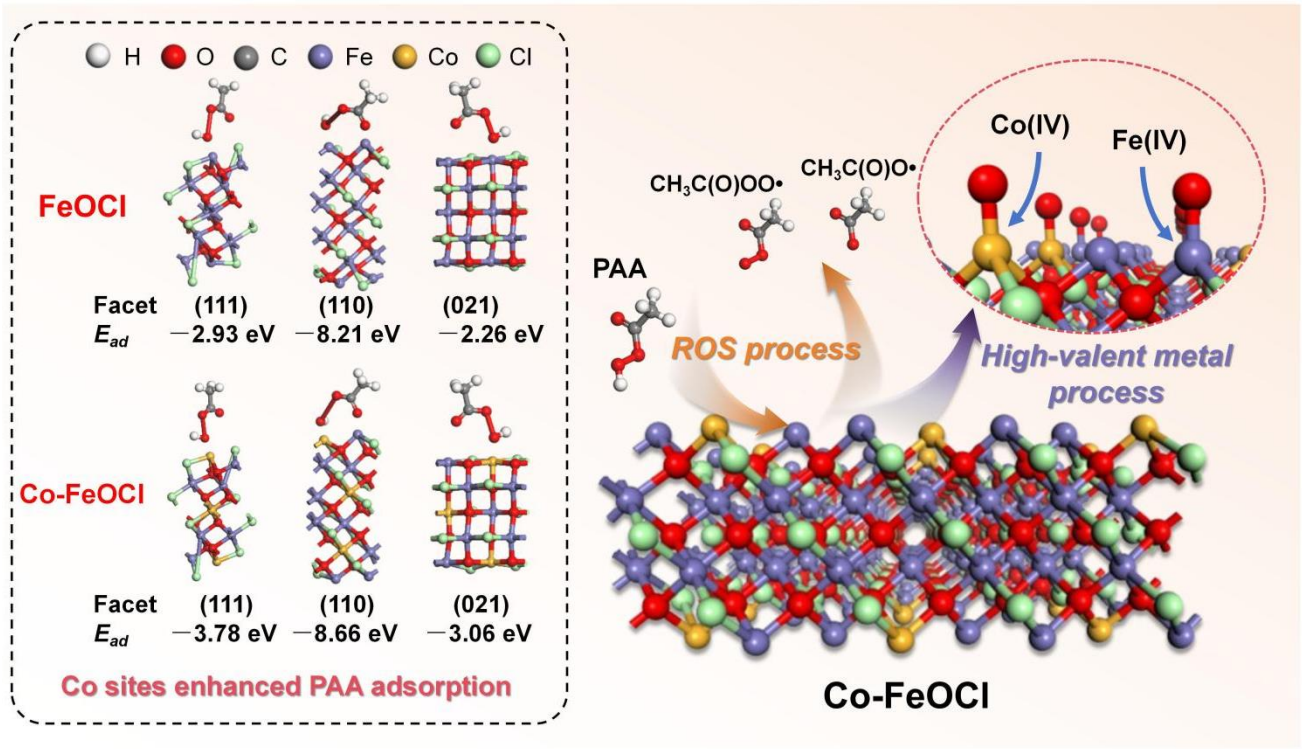
Hu, J., **Zhang, H.**, Xia, S., Cai, Y., Shi, Z., Deng, J. (2026):
Harnessing the Co-Fe synergy: A novel Co-doped FeOCl for peracetic acid activation to efficiently degrade carbamazepine
Colloid Surf. A-Physicochem. Eng. Asp. **742, Part 1** , art. 140410

The publisher's version is available at:

https://doi.org/10.1016/j.colsurfa.2026.140410

Click here to access/download;Graphical Abstract (for review);Graphical Abstract.docx

Graphical abstract



Highlights

- A Co-doped FeOCl catalyst was synthesized to overcome the slow Fe(III)/Fe(II) cycle inherent in pure FeOCl.
- The optimized 0.5Co-FeOCl/PAA system achieved a reaction rate 5.6 times higher than the FeOCl/PAA system.
- CBZ degradation was driven by organic radicals and high-valent Fe(IV)/Co(IV) species.
- DFT calculations revealed that Co sites exhibit stronger affinity for PAA adsorption compared to Fe sites.

Manuscript Click here to access/download;Manuscript;Manuscript.docx

Click here to view linked References

Cobalt-doped FeOCl for peracetic acid activation toward carbamazepine degradation: Crystal facet regulation and Co–Fe synergy

Jinlin Hu[a], Haojie Zhang[a,b,*], Simeng Xia[a], Zhou Shi[a], Lin Deng[a,*]

a. Key Laboratory of Building Safety and Energy Efficiency, Ministry of Education, College of Civil Engineering, Hunan University, Changsha 410082, China

b. Department of Technical Biogeochemistry, Helmholtz Centre for Environmental Research – UFZ, Leipzig 04318, Germany

*Corresponding authors

E-mail addresses: zhj95@hnu.edu.cn (H. Zhang); lindeng@hnu.edu.cn (L. Deng)

Abstract

The widespread occurrence of carbamazepine (CBZ) in aquatic environments necessitates efficient water treatment technologies. This study developed a cobalt-doped iron oxychloride (Co-FeOCl) catalyst via a facile calcination method to activate peracetic acid (PAA) for enhanced degradation of CBZ. The incorporation of Co into the FeOCl structure dramatically boosted the catalytic performance, with 0.5Co-FeOCl exhibiting superior activity compared to pristine FeOCl. The 0.5Co-FeOCl/PAA system achieved an apparent rate constant of 0.039 min^{-1}, 19.5 and 5.6 times higher than that of the PAA alone (0.002 min^{-1}) and FeOCl/PAA (0.007 min^{-1}) systems, respectively. Mechanistic investigations revealed that the degradation was primarily driven by organic radicals ($CH_3C(O)OO•$ and $CH_3C(O)O•$) and high-valent metal species (Co(IV) and Fe(IV)). The Co doping established synergistic Fe(II)/Fe(III)-Co(II)/Co(III) redox cycles, effectively accelerating the rate-limiting Fe(III) reduction step and facilitating continuous generation of reactive species. XPS analysis confirmed an increased surface Fe(II) content after reaction, supporting this synergistic mechanism. Density functional theory (DFT) calculations proved that Co sites exhibit superior adsorption capacity for PAA compared to Fe sites on three main facets. This work not only presents 0.5Co-FeOCl as a highly efficient and stable catalyst for PAA activation but also provides fundamental insights into the synergistic mechanisms in bimetallic/PAA systems for remediating refractory organic pollutants.

Keywords: Co-doped FeOCl; Peracetic acid; Carbamazepine degradation; Advanced oxidation processes; Synergistic mechanism

1. Introduction

Pharmaceuticals and personal care products have emerged as a pervasive class of trace organic pollutants, increasingly detected in diverse environmental matrices, including drinking water. Among them, carbamazepine (CBZ), a widely prescribed anticonvulsant for epilepsy and trigeminal neuralgia [1], is of particular concern due to its high persistence, potential for bioaccumulation, and resistance to degradation, even after metabolic excretion, thereby posing significant risks to aquatic ecosystems and human health [2, 3].

Various water treatment technologies have been explored to address this issue, including membrane filtration [4], electrochemical treatment [5], adsorption [6], and advanced oxidation processes (AOPs) [7]. Owing to their capacity to generate highly reactive oxygen species (ROS) capable of mineralizing pollutants or converting them into less toxic byproducts, AOPs represent a particularly promising solution [8]. Recently, peracetic acid (PAA) has gained traction as a superior alternative to conventional AOP precursors like peroxymonosulfate (PMS), H_2O_2, and persulfate, owing to its lower O–O bond energy, which facilitates more efficient activation [9]. Upon activation, PAA can produce a diverse array of reactive species [10, 11], including hydroxyl radical (•OH) and organic radical (R-O•) [12, 13], driving the development of efficient PAA-based AOPs for water decontamination [14-18].

PAA activation can be achieved by multiple methods, including ultraviolet irradiation [19], thermal energy [20], and transition metals (e.g., Co, Cu, Mn, Fe) [21, 22]. Among these, transition metal-based activation is highly suited for large-scale

applications due to its high catalytic efficiency, broad applicability, and energy-independent operation. Iron species (e.g., Fe^{2+}, Fe^{3+}) are widely employed owing to their low toxicity and effectiveness. However, homogeneous Fe-catalyzed systems are plagued by inherent drawbacks, including significant oxidant scavenging, stringent pH dependence, difficulties in catalyst recovery, and the risk of secondary pollution from residual iron ions. These limitations elevate operational costs and potential environmental risks, underscoring the critical need to develop efficient, eco-friendly, and reusable solid iron-based catalysts.

Two-dimensional layered metal oxychlorides, such as FeOCl and BiOCl, have recently attracted considerable interest in catalysis due to their unique coordination structures, strong visible-light absorption, and high structural tunability [23, 24]. FeOCl, featuring characteristic linear Cl–Fe–O and Fe–O–Fe configuration, exposes a higher density of unsaturated iron sites on its surface compared to conventional iron oxides (e.g., Fe_2O_3 and Fe_3O_4), thereby enhancing its catalytic potential [25, 26]. Despite this advantage, the practical application of FeOCl is substantially hampered by the sluggish regeneration of Fe(II) from Fe(III), which severely restricts its degradation kinetics and overall efficacy [27]. Heteroatom doping has emerged as a powerful strategy to overcome this kinetic limitation. Recent studies confirm that bimetallic catalysts often exhibit superior performance due to synergistic inter-metal effects [28]. Consequently, doping FeOCl with metals such as Zn [29], Sn [30], or Cu [31] has proven effective in boosting its catalytic activity. Notably, cobalt (Co) stands out among transition metals for PAA activation, given its versatile redox chemistry

(Co^{2+}/Co^{3+}), efficient electron transfer capability, and ability to modulate oxygen vacancy density.

Inspired by these insights, we designed and synthesized a novel Co-doped FeOCl (Co-FeOCl) catalyst via a facile calcination method. We hypothesize that introducing Co will establish synergistic Fe(II)/Fe(III)-Co(II)/Co(III) redox cycles, thereby accelerating the rate-limiting Fe(III) reduction step and enhancing the overall catalytic performance. Nevertheless, research on PAA activation by Co-FeOCl remains scarce, and the underlying mechanisms governing its efficacy are still elusive.

Therefore, this study aims to construct a Co-FeOCl/PAA system for CBZ degradation. The specific objectives are to: (i) optimize the synthesis parameters of Co-FeOCl; (ii) evaluate the effects of key operational conditions (e.g., initial pH, catalyst and PAA dosages, and common anions) on CBZ removal; (iii) identify the dominant reactive species and quantify their contributions; (iv) elucidate the structure-activity relationship of the catalyst and the PAA activation mechanism; and (v) propose potential CBZ degradation pathways and assess the toxicity evolution of its transformation products.

2. Materials and methods

2.1. Chemicals

All reagents were of analytical grade and used without further purification. PAA (10 wt% in water), $FeCl_3·6H_2O$, $CoCl_2·6H_2O$, $NiCl_2·6H_2O$, $MnCl_2·4H_2O$, $ZnCl_2$, $CuCl_2$, H_2SO_4, NaOH, NaCl, Na_2SO_4, $NaHCO_3$, Na_2CO_3, and H_2O_2 were obtained from Aladdin Scientific Co., Ltd. (Shanghai, China). CBZ, sulfamethoxazole (SMX),

sulfadiazine (SDZ), and tetracycline (TC), methanol (MeOH), tert-butanol (TBA), p-benzoquinone (BQ), 2,4-hexadiene (2,4-HD), furfuryl alcohol (FFA), phenyl methyl sulfoxide (PMSO), methyl phenyl sulfone ($PMSO_2$), 5,5-Dimethyl-1-pyrroline N-oxide (DMPO), and 2,2,6,6-tetramethyl-4-piperidone (TEMP) were purchased from Sigma-Aladdin Chemical Co., Ltd (Shanghai, China). Ultrapure water (18.2 MΩ·cm) was generated by a Millipore system (Bedford, USA).

2.2. Synthesis of Co-FeOCl

The *x*Co-FeOCl catalysts were synthesized using a one-step calcination method. Specifically, varying amounts of $FeCl_3·6H_2O$ and $CoCl_2·6H_2O$ were dissolved in 4 mL of ultrapure water and sonicated for 30 min at room temperature. The mixture was then dried in an oven at 70 ℃ for 24 h. Subsequently, the dried solid was transferred to a muffle furnace, heated to 250 ℃ at a rate of 10 ℃/min, and held at that temperature for 2.5 h. After cooling naturally to room temperature, the product was thoroughly washed with methanol and deionized water, dried, and ground to obtain the final *x*Co-FeOCl material. Based on the molar ratios of $CoCl_2·6H_2O$ to $FeCl_3·6H_2O$ (1:10, 1:5, 3:10, and 2:5), the resulting catalysts were designated as 0.5Co-FeOCl, 1.0Co-FeOCl, 1.5Co-FeOCl, and 2.0Co-FeOCl, respectively. For comparison, Ni-, Mn-, Cu-, Zn-doped FeOCl were synthesized using the same procedure.

2.3. Experimental procedure

Catalytic degradation experiments were conducted at ambient temperature in batch mode. A 50 mL CBZ solution was prepared in a 100 mL beaker by diluting a

stock solution with ultrapure water. A specified dosage of Co-FeOCl catalyst was added, and the mixture was stirred for 10 min to achieve adsorption–desorption equilibrium. The reaction was initiated by rapidly adding the PAA solution. Subsequently, 0.5 mL aliquots were collected at prescribed time intervals (0, 10, 20, 30, 40, 50, and 60 min), immediately filtered through 0.22 μm membranes, and quenched with an equal volume of methanol for analysis. If necessary, the initial pH of the solution was adjusted to a pre-determined value using 0.1 M H_2SO_4 or 0.1 M NaOH. The solution pH was measured by a pH meter (PHS-3C, INESA Scientific Instrument, China). The relative standard deviation was consistently below 5%. Quenching experiments were carried out by adding MeOH, BQ, TBA, FFA, Mn^{2+}, PMSO, and 2,4-HD as scavengers. All degradation experiments were performed in triplicate.

2.4. Catalysts characterization and analytical methods

Scanning electron microscopy (SEM, ZEISS Sigma 300) was used to examine the surface morphology. High-resolution transmission electron microscopy (HRTEM, Thermo Fisher Talos F200X G2) and energy-dispersive X-ray spectroscopy (EDX, JEM-2100F) were employed to analyze microstructure and elemental distribution. X-ray diffraction (XRD, D8 Advance, Bruker) with Ni-filtered Cu Kα radiation (scan rate: 0.02°/s in 2θ) was performed to determine crystallinity and phase composition. X-ray photoelectron spectroscopy (XPS, Thermo Scientific K-Alpha) was conducted to analyze surface elemental composition and chemical states. Fourier transform infrared spectroscopy (FTIR, Thermo Fisher Scientific Nicolet iS20) was used to

identify functional groups. Element content was analyzed by inductively coupled plasma mass spectrometer (ICP-OES, Agilent 7800MS). The electron spin resonance (ESR) spectra were recorded by an ESR spectrometer (Bruker EMXnano, Germany).

Analytical details are provided in Text S1 (Supplementary Material). The concentration of CBZ was measured by high-performance liquid chromatography (HPLC, Waters 2695) equipped with diode array detector (PDA waters 2998) and fluorescence detector (Waters 2475). An Waters symmetry C18 column (4.6 mm × 150 mm, 5 μm particle size) was used. The HPLC analysis parameters for CBZ, SMX, SDZ, TC, PMSO, $PMSO_2$ are listed in Table S1.

3. Results and discussion

3.1. Optimization of synthesis parameters for *x*-Co-FeOCl

The catalytic activities of various transition metal-doped FeOCl catalysts (M-FeOCl, M = Co, Ni, Mn, Cu, Zn) were evaluated for PAA activation. As shown in Figure 1a, the Co-FeOCl/PAA system exhibited superior performance, achieving over 90% degradation of CBZ within 60 min using 0.1 g/L of Co-FeOCl and 0.6 mM of PAA. In contrast, Ni-, Mn-, Cu-, and Zn-doped FeOCl catalysts showed moderate to low activities. The remarkable efficiency of Co-FeOCl is attributed to the strong redox capability of cobalt and its synergistic effect with iron, promoting efficient PAA activation. The apparent first-order rate constants (k_{obs}) followed the order: Co-FeOCl (0.039 min^{-1}) > Ni-FeOCl (0.027 min^{-1}) > Mn-FeOCl (0.011 min^{-1}) > Cu-FeOCl (0.004 min^{-1}) > Zn-FeOCl (0.003 min^{-1}) (Figure S1).

Control experiments confirmed the necessity of both the catalyst and the oxidant. As depicted in Figure 1b, negligible CBZ removal was observed with PAA alone or 0.5Co-FeOCl alone. The FeOCl/PAA system achieved only 31.5% removal after 60 min. In sharp contrast, the 0.5Co-FeOCl/PAA system removed over 90% of CBZ within the same timeframe, highlighting the synergy between Co doping and PAA activation. The k_{obs} value for the 0.5Co-FeOCl/PAA system (0.039 min^{-1}) was 19.5 and 5.6 times higher than those of PAA alone (0.002 min^{-1}) and FeOCl/PAA (0.007 min^{-1}) (Figure S2), respectively. These results clearly demonstrate that Co doping significantly enhances the catalytic activity of FeOCl and that PAA activation is the primary pathway for CBZ degradation.

The influence of Co doping content was further investigated. As shown in Figure 1c, the catalytic activity of *x*Co-FeOCl was highly dependent on the doping ratio, with an optimal concentration yielding the highest degradation efficiency. Both lower and higher doping levels reduced performance, indicating the importance of balancing the number of active sites and electron transfer efficiency. Catalyst stability was assessed by measuring metal leaching (Fe and Co). Figure 1d shows that the leached Fe concentration remained consistently low (0.5–0.6 mg/L) across all samples, while Co leaching increased significantly with higher doping levels. Considering both activity and environmental safety, 0.5Co-FeOCl was selected for further study.

3.2. Catalysts characterizations

The surface morphology of the as-synthesized catalysts was examined by SEM and TEM. As shown in Figure 2a and b, both FeOCl and 0.5Co-FeOCl display a flat,

smooth surface composed of well-defined solid flakes (4–18 μm in length) stacked in a layered architecture (Figure 2c), which is characteristic of the FeOCl structure. EDS elemental mapping (Figure 2d) confirms the homogeneous distribution of Co, Fe, O, and Cl throughout the 0.5Co-FeOCl sample. XRD analysis (Figure 2e) shows that the pristine FeOCl exhibits distinct diffraction peaks at 2θ = 24.3°, 34.0°, 36.0°, 41.2°, 49.9°, 54.6°, 62.6°, and 64.4°, corresponding to the (110), (021), (111), (130), (131), (002), (221), and (150) crystal planes, respectively. These peaks match well with the standard reference pattern for β-FeOCl (JCPDS No. 24-1005), confirming the successful formation of a crystalline FeOCl phase. Importantly, the introduction of Co did not induce significant changes, and 0.5Co-FeOCl retained the fundamental FeOCl framework, with sharp and intense diffraction peaks indicating high crystallinity. FTIR spectra was collected to compare the functional groups present in pure FeOCl and 0.5Co-FeOCl (Figure 2f). Both samples exhibit a broad absorption band around 3418.0–3421.8 cm^{-1}, potentially indicating the presence of very strongly hydrogen-bonded or distinct metal–hydroxyl (M–OH) environments. As for the 0.5Co-FeOCl, the band at 1606.4 cm^{-1} can correspond to H–O–H bending vibrations of adsorbed water. The band at 1371.3 cm^{-1} is related to deformation vibrations of metal–bonded hydroxyl groups (M–OH). The peak at 804.7 cm^{-1} likely arises from metal-oxygen stretching vibrations. It could be associated with the formation of Co–O bonds or modified Fe–O bonds within the lattice. The absorption bands below 750 cm^{-1} are characteristic of metal-oxygen (M–O) stretching vibrations in metal oxide lattices. In the XPS Cl 2p spectra (Figure 2g), 0.5Co-FeOCl exhibits peaks at binding

energies of 198.9 eV (Cl $2p_{3/2}$) and 200.5 eV (Cl $2p_{1/2}$), corresponding to the covalent Fe–Cl bonds. The Fe 2p spectra (Figure 2h) shows coexisting Fe(II) (711.2 eV and 723.9 eV) and Fe(III) (726.1 eV and 712.4 eV).

In conclusion, SEM, TEM, XRD, FTIR, and XPS analyses confirm the successful synthesis of 0.5Co-FeOCl catalyst while perfectly preserving the parent FeOCl crystal structure.

3.3. Influence of key operational parameters on CBZ removal

The efficacy of the 0.5Co-FeOCl/PAA system was evaluated under various operational parameters. As shown in Figure 3a, CBZ degradation exhibited a positive correlation with catalyst dosage (0.04 to 0.20 g/L). The highest dosage (0.20 g/L) achieved near-complete CBZ removal within 30 min, indicating a surface-reaction limited process under these conditions. Similarly, increasing PAA concentration from 0.3 mM to 1.5 mM enhanced CBZ removal from 61.2% to 100% (Figure 3b), underscoring the critical role of oxidant availability.

The initial solution pH also exerted a profound influence (Figure 3c). The removal of CBZ by the 0.5Co-FeOCl/PAA system was strongly suppressed at pH 3.0, peaked at over 90% removal at neutral pH (7.0), and declined to 53.4% at pH 9.0. This pH-dependent behavior is attributed to catalyst surface charge and PAA speciation. In acidic media, protonated PAA experiences electrostatic repulsion with positively charged active sites (Co^{2+}, Fe^{2+}), hindering electron transfer and the formation of reactive species [32]. The decreased performance under alkaline

conditions is primarily related to PAA self-decomposition and inactive iron/cobalt hydroxide precipitates formation [32-34].

The influence of common coexisting inorganic anions (Cl^-, SO_4^{2-}, HCO_3^-, CO_3^{2-}) on CBZ degradation is presented in Figure 3d. A significant inhibitory effect was observed in the presence of HCO_3^- and CO_3^{2-}, which can be ascribed to multiple mechanisms: (i) their hydrolysis increases the solution pH, creating unfavorable alkaline conditions; (ii) they act as scavengers of reactive peroxygen species [35, 36]; and they may form surface complexes that passivate active sites [33]. In contrast, Cl^- and SO_4^{2-} exhibited only minor effects, with CBZ removal remaining comparable to the anion-free control. This marked contrast highlights the critical role of carbonate species in determining the system's applicability in complex water matrices. To gauge its practical potential, the system underwent evaluation using SMX, SDZ, and TC, common antibiotic pollutants exhibiting diverse molecular structures. As shown in Figure S3, over 90% removal of each compound was achieved within 60 min, demonstrating the strong effectiveness and broad applicability of the 0.5Co-FeOCl/PAA system for degrading diverse organic pollutants in water treatment. XRD patterns of fresh and used 0.5Co-FeOCl showed no detectable structural changes (Figure S4), attesting to the catalyst's stability.

3.4. Mechanisms for CBZ degradation in the 0.5Co-FeOCl/PAA system

3.4.1 Identification of reactive species

PAA-based AOPs can generate a diverse range of reactive species capable of degrading organic pollutants, including •OH, O_2•$^-$, $^1O_2$, and organic radicals such as

acetylperoxy ($CH_3C(O)O•$), peracetyl ($CH_3C(O)OO•$), methylperoxy ($CH_3OO•$), and methyl ($CH_3•$) radicals [37]. To identify the dominant reactive species, quenching experiments were performed using several scavengers: MeOH for •OH and organic radicals; TBA as a selective •OH quencher (k = 3.8–7.6×10^8 M^{-1} s^{-1}); 2,4-HD and Mn^{2+} for $CH_3C(O)O•$ and $CH_3C(O)OO•$, respectively; BQ for $O_2•^-$ (k = 2.9×10^9 $M^{-1}s^{-1}$); FFA for both •OH (k = 1.5×10^{10} $M^{-1}s^{-1}$) and $^1O_2$ (k = 1.2×10^8 M^{-1} s^{-1}); and PMSO for high-valent metal–oxo species. As shown in Figure 4a, the addition of MeOH (50 mM) caused the most striking inhibition (5.6% CBZ removal). TBA (50 mM) reduced the removal to 71.3%, implicating the contribution of both •OH and organic radicals, with the latter exerting a more dominant influence. BQ and FFA slashed efficiency to 44.6% and 50.3%, respectively, confirming the participation of $O_2•^-$ and $^1O_2$. 2,4-HD and Mn^{2+} markedly reduced the degradation to 22.3% and 19.1%, highlighting the crucial contribution of $CH_3C(O)O•$ and $CH_3C(O)OO•$. Also, PMSO profoundly inhibited the degradation (15.5% removal), underscoring the role of high-valent metal–oxo species.

Electron paramagnetic resonance (EPR) spectroscopy can provide direct evidence of radical generation. As shown in Figure 4b-c, characteristic signals of DMPO-ROO•, DMPO-•OH, and TEMP-$^1O_2$ adducts were detected, confirming the formation of ROO•, •OH, and $^1O_2$ [38, 39]. To probe high-valent metal species, we employed PMSO, a substrate selectively oxidized to $PMSO_2$ by high-valent metal-oxo species [32]. As shown in Figure 4d, 37.7% of PMSO was consumed over 60 min, with 44.8% of the consumed amount stoichiometrically converted to $PMSO_2$ (1.69

μM), providing compelling evidence for the involvement of high-valent Fe(IV)/Co(IV) species.

In summary, CBZ degradation in the 0.5Co-FeOCl/PAA system was driven by multiple reactive species, with organic radicals ($CH_3C(O)OO•$/$CH_3C(O)O•$) and high-valent Fe(IV)/Co(IV) playing major roles.

3.4.2 XPS analysis of 0.5Co-FeOCl before and after reaction

XPS analysis probed the evolution of chemical states in 0.5Co-FeOCl during the catalytic reaction (Figure 5). The Fe–Cl peak in the Cl 2p spectra remained observable in the used catalyst, confirming structural stability (Figure 5a) [40]. In the O 1s spectra (Figure 5b), three distinct components were identified: lattice oxygen (O_L, 530.5 eV), surface hydroxyl groups (O_A, 531.9 eV), and physically adsorbed H_2O (O_H, 532.3 eV). After reaction, the O_L content surged from 14.2% to 39.4%, while O_A plummeted from 59.9% to 9.9%, and O_H increased from 25.9% to 50.7%. This transformation indicates direct involvement of surface hydroxyl groups in the catalytic process. Deconvolution of the Fe $2p_{3/2}$ region (Figure 5c) revealed Fe(II) (711.1 eV) and Fe(III) (712.6 eV) [40, 41], with relative contents of 36.19% and 63.81%, respectively [42]. After catalytic, the peaks shifted to lower binding energies (711.3 eV and 724.9 eV, respectively), and the Fe(II) content increased to 70.71% in the Fe $2p_{3/2}$ region, strongly supporting the involvement of iron redox cycling [43]. The Co 2p spectrum (Figure 5d) exhibited an atypical line shape, attributable to low cobalt loading and an elevated background signal [44, 45].

3.4.3 DFT calculations of PAA adsorption on various facets

To further elucidate the role of doped Co atoms, DFT calculations were performed to investigate the adsorption of PAA on the dominant facets of FeOCl and 0.5Co-FeOCl (see Text S2 for details). Based on XRD analysis, the (111), (110), and (021) facets were identified as the predominant facets for both materials. The optimized adsorption configurations of PAA on these facets of FeOCl and 0.5Co-FeOCl are shown in Figure 5e and f, respectively. In all cases, the Fe and Co metal sites act as the primary adsorption centers for PAA. The calculated adsorption energies (E_{ad}) of PAA on the (111), (110), and (021) facets of FeOCl are –2.93, –8.21, and –2.26 eV, respectively. For 0.5Co-FeOCl, the corresponding E_{ad} values are –3.78, –8.66, and –3.06 eV. The (110) facet exhibits notably stronger adsorption, which can be attributed to its higher density of exposed metal sites. Importantly, across all three facets, Co sites show higher affinity for PAA adsorption compared to Fe sites, highlighting the crucial role of Co in promoting PAA activation. Differential charge density analysis further reveals that the amount of charge transfer follows the same trend as the adsorption energy. The (110) facet demonstrates the largest charge transfer, with values of 0.70 e^- for FeOCl and 0.72 e^- for 0.5Co-FeOCl. Moreover, charge transfer from Co sites to PAA consistently exceeds that from Fe sites. These results strongly corroborate the significant contribution of Co doping to PAA activation at the atomic level.

3.4.4 Proposed degradation pathways of CBZ

The degradation pathway of CBZ in the 0.5Co-FeOCl/PAA system was investigated by identifying thirteen intermediates via liquid chromatography–mass

spectrometry (LC–MS) (Table S2). As shown in Figure 6, three primary degradation routes are proposed, initiated by reactive species (primarily organic radicals, Fe(IV), and Co(VI)). In Pathway I, the central C=C double bond of CBZ undergoes hydroxylation, forming P1 (m/z 253). This intermediate is further oxidized, leading to dihydroxylated (e.g., P2, m/z 271) or ketone derivatives (e.g., P3, m/z 269) via subsequent attacks on the azepine ring. Pathway II involves more extensive structural destruction, culminating in azepine ring opening. CBZ or its hydroxylated derivatives (e.g., P1) undergo ring rearrangement and contraction, often accompanied by decarboxylation (–CO_2) or loss of the –$CONH_2$ group, to yield the six-membered ring intermediate P6 (m/z 210). Subsequent oxidative cleavage of this contracted ring generates smaller fragments such as P7 (m/z 180) and P8 (m/z 251). Ultimately, the cleavage products are subjected to further radical attacks, breaking C–N and C–C bonds and yielding a series of low-molecular-weight carboxylic acids. This is evidenced by the detection of P9 (m/z 198) and P4 (m/z 224) from partial cleavage; P10 (m/z 139) and P11 (m/z 123) from further fragmentation; and finally, P12 (m/z 111) and P13 (m/z 99), which represent the ultimate products before mineralization (e.g., succinic, oxaloacetic, or oxalic acid derivatives). These small acids can ultimately be mineralized to CO_2 and H_2O [46-48].

3.4.5 Proposed mechanisms for CBZ degradation in the 0.5Co-FeOCl/PAA system

A proposed catalytic mechanism for CBZ degradation in the 0.5Co-FeOCl/PAA system is illustrated in Figure 7. The process is driven by the redox cycling of Fe(II)/Fe(III) and Co(II)/Co(III), which facilitates the generation of radicals species

and high-valent Fe(IV) and Co(IV) species. Initially, surface Fe(II) and Co(II) sites on the catalyst coordinate with adsorbed PAA, forming Fe(II)–PAA and Co(II)–PAA complexes. These complexes undergo intramolecular electron transfer, decomposing to produce Fe(III) and Co(III) alongside the $CH_3C(O)O•$ radicals. The resulting Fe(III) and Co(III) can subsequently complex with another PAA molecule (forming Fe(III)–PAA and Co(III)–PAA) and be reduced back to Fe(II) and Co(II), thereby generating $CH_3C(O)OO•$. Alternatively, the Fe(II)–PAA and Co(II)–PAA complexes may proceed via a two-electron transfer pathway, directly yielding highly oxidizing Fe(IV) and Co(IV) species.

4. Conclusions

In this study, a Co-doped FeOCl catalyst was successfully synthesized and employed to activate PAA for the efficient degradation of CBZ. Co doping significantly enhanced the catalytic activity of FeOCl. The optimized 0.5Co-FeOCl/PAA system achieved excellent CBZ removal, substantially outperforming pure FeOCl and other transition-metal-doped FeOCl catalysts, highlighting the unique synergy between Co and Fe. Notably, 0.5Co-FeOCl exhibited a favorable balance between high catalytic activity and low metal leaching, suggesting its potential for practical application. Mechanistic investigations revealed that the system operated through a unique combination of organic radicals ($CH_3C(O)OO•$/$CH_3C(O)O•$) and high-valent Fe(IV)/Co(IV) species. The introduction of Co efficiently promoted the regeneration of Fe(II) from Fe(III), establishing a synergistic catalytic cycle that enhanced PAA activation. DFT calculations further

indicated that Co sites possess superior PAA adsorption capacity over Fe sites on three dominant (111), (110) and (021) facets. Based on intermediates analysis, possible degradation pathways involving hydroxylation, ring contraction, and bond cleavage were proposed. This work not only presents 0.5Co-FeOCl as a highly effective catalyst for PAA-based AOPs, but also offers fundamental insight into the synergistic mechanisms in bimetallic/PAA systems, thereby supporting their future application for eliminating persistent organic pollutants from water.

Acknowledgments

This work was financially supported by National Natural Science Foundation of China (52270004).

References

[1] S. Remy, S. Gabriel, B.W. Urban, D. Dietrich, T.N. Lehmann, C.E. Elger, U. Heinemann, H. Beck, A novel mechanism underlying drug resistance in chronic epilepsy, Annals of Neurology 53(4) (2003) 469–479. https://doi.org/https://doi.org/10.1002/ana.10473.

[2] L. Bo, K. He, N. Tan, B. Gao, Q. Feng, J. Liu, L. Wang, Photocatalytic oxidation of trace carbamazepine in aqueous solution by visible-light-driven Znln2S4: Performance and mechanism, Journal of Environmental Management 190 (2017) 259–265. https://doi.org/10.1016/j.jenvman.2016.12.050.

[3] R. Moreno-González, S. Rodríguez-Mozaz, M. Gros, E. Pérez-Cánovas, D. Barceló, V.M. León, Input of pharmaceuticals through coastal surface watercourses into a Mediterranean lagoon (Mar Menor, SE Spain): Sources and seasonal variations, Science of The Total Environment 490 (2014) 59–72. https://doi.org/10.1016/j.scitotenv.2014.04.097.

[4] Z. Liao, M.N. Nguyen, G. Wan, J. Xie, L. Ni, J. Qi, J. Li, A.I. Schäfer, Low pressure operated ultrafiltration membrane with integration of hollow mesoporous carbon nanospheres for effective removal of micropollutants, Journal of Hazardous Materials 397 (2020). https://doi.org/10.1016/j.jhazmat.2020.122779.

[5] C. Dai, D. Chen, J. Wu, J. Liu, S. Shi, J. Zhang, Y. Feng, Construction of a novel integrated electrochemical oxidation-coagulation system for simultaneous removal of suspended solids and antibiotics, Chemical Engineering Journal 447 (2022). https://doi.org/10.1016/j.cej.2022.137505.

[6] P. Liu, Q. Wang, C. Zheng, C. He, Sorption of Sulfadiazine, Norfloxacin, Metronidazole, and Tetracycline by Granular Activated Carbon: Kinetics, Mechanisms, and Isotherms, Water, Air, & Soil Pollution 228(4) (2017). https://doi.org/10.1007/s11270-017-3320-x.

[7] Y. Zhang, Y.-G. Zhao, F. Maqbool, Y. Hu, Removal of antibiotics pollutants in wastewater by UV-based advanced oxidation processes: Influence of water matrix components, processes optimization and application: A review, Journal of Water Process Engineering 45 (2022). https://doi.org/10.1016/j.jwpe.2021.102496.

[8] A.V. Karim, A. Hassani, P. Eghbali, P.V. Nidheesh, Nanostructured modified layered double hydroxides (LDHs)-based catalysts: A review on synthesis, characterization, and applications in water remediation by advanced oxidation processes, Current Opinion in Solid State and Materials Science 26(1) (2022). https://doi.org/10.1016/j.cossms.2021.100965.

[9] T. Luukkonen, S. Pehkonen, Peracids in water treatment: A critical review, Critical Reviews in Environmental Science and Technology 47(1) (2017) 1–39. https://doi.org/10.1080/10643389.2016.1272343.

[10] F. Chen, L. Liu, J. Wu, X. Rui, J. Chen, Y. Yu, Single-Atom Iron Anchored Tubular g-C3N4 Catalysts for Ultrafast Fenton-Like Reaction: Roles of High-Valency Iron-Oxo Species and Organic Radicals, Advanced Materials 34(31) (2022). https://doi.org/10.1002/adma.202202891.

[11] T. Yang, L. An, G. Zeng, M. Jiang, J. Li, C. Liu, J. Jia, J. Ma, Efficient removal of p-arsanilic acid and arsenite by Fe(II)/peracetic acid (Fe(II)/PAA) and PAA processes, Water Research 241 (2023). https://doi.org/10.1016/j.watres.2023.120091.

[12] J. Hollman, J. Dominic, G. Achari, Degradation of pharmaceutical mixtures in aqueous solutions using UV/peracetic acid process: Kinetics, degradation pathways and comparison with UV/H2O2, Chemosphere 248 (2020). https://doi.org/10.1016/j.chemosphere.2020.125911.

[13] W. Sun, K. Pang, F. Ye, M. Pu, C. Zhou, H. Huang, Q. Zhang, J. Niu, Carbonization of camphor sulfonic acid and melamine to N,S-co-doped carbon for sulfamethoxazole degradation via persulfate

activation: Nonradical dominant pathway, Separation and Purification Technology 279 (2021). https://doi.org/10.1016/j.seppur.2021.119723.
[14] C. Zhang, P. Brown, Z. Hu, Thermodynamic properties of an emerging chemical disinfectant, peracetic acid, Science of the Total Environment 621 (2018) 948–959. https://doi.org/10.1016/j.scitotenv.2017.10.195.
[15] J. Lee, U. von Gunten, J. Kim, Persulfate-Based Advanced Oxidation: Critical Assessment of Opportunities and Roadblocks, Environmental Science & Technology 54(6) (2020) 3064–3081. https://doi.org/10.1021/acs.est.9b07082.
[16] X. Ao, J. Eloranta, C. Huang, D. Santoro, W. Sun, Z. Lu, C. Li, Peracetic acid-based advanced oxidation processes for decontamination and disinfection of water: A review, Water Research 188 (2021). https://doi.org/10.1016/j.watres.2020.116479.
[17] D. Miklos, C. Remy, M. Jekel, K. Linden, J. Drewes, U. Hübner, Evaluation of advanced oxidation processes for water and wastewater treatment - A critical review, Water Research 139 (2018) 118–131. https://doi.org/10.1016/j.watres.2018.03.042.
[18] M. Priyadarshini, I. Das, M. Ghangrekar, L. Blaney, Advanced oxidation processes: Performance, advantages, and scale-up of emerging technologies, Journal of Environmental Management 316 (2022). https://doi.org/10.1016/j.jenvman.2022.115295.
[19] W. Wu, D. Tian, T. Liu, J. Chen, T. Huang, X. Zhou, Y. Zhang, Degradation of organic compounds by peracetic acid activated with Co3O4: A novel advanced oxidation process and organic radical contribution, Chemical Engineering Journal 394 (2020). https://doi.org/10.1016/j.cej.2020.124938.
[20] J. Wang, Y. Wan, J. Ding, Z. Wang, J. Ma, P. Xie, M. Wiesner, Thermal Activation of Peracetic Acid in Aquatic Solution: The Mechanism and Application to Degrade Sulfamethoxazole, Environmental Science & Technology 54(22) (2020) 14635–14645. https://doi.org/10.1021/acs.est.0c02061.
[21] J. Dong, W. Xu, S. Liu, Y. Gong, T. Yang, L. Du, Q. Chen, X. Tan, Y. Liu, Lignin-derived biochar to support CoFe2O4: Effective activation of peracetic acid for sulfamethoxazole degradation, Chemical Engineering Journal 430 (2022). https://doi.org/10.1016/j.cej.2021.132868.
[22] J. Kim, P. Du, W. Liu, C. Luo, H. Zhao, C. Huang, Cobalt/Peracetic Acid: Advanced Oxidation of Aromatic Organic Compounds by Acetylperoxyl Radicals, Environmental Science & Technology 54(8) (2020) 5268–5278. https://doi.org/10.1021/acs.est.0c00356.
[23] J. Wang, Y. Li, Q. Jiang, S. Tong, Study on why FeOCl has high Fenton activity in wide range of initial pH and its corresponding stability, Process Safety and Environmental Protection 172 (2023) 652–658. https://doi.org/10.1016/j.psep.2023.02.050.
[24] C. Tan, Q. Xu, T. Sheng, X. Cui, Z. Wu, H. Gao, H. Li, Reactive oxygen species generation in FeOCl nanosheets activated peroxymonosulfate system: Radicals and non-radical pathways, Journal of Hazardous Materials 398 (2020). https://doi.org/10.1016/j.jhazmat.2020.123084.
[25] Y. Cao, K. Cui, Y. Chen, M. Cui, G. Li, D. Li, X. Yang, Efficient degradation of tetracycline by H2O2 catalyzed by FeOCl: A wide range of pH values from 3 to 7, Solid State Sciences 113 (2021). https://doi.org/10.1016/j.solidstatesciences.2021.106548.
[26] V. Nguyen, M. Mousavi, J. Ghasemi, Q. Le, S. Delbari, M. Asl, M. Shokouhimehr, M. Mohammadi, Y. Azizian-Kalandaragh, A. Namini, In situ preparation of g-C3N4 nanosheet/FeOCl: Achievement and promoted photocatalytic nitrogen fixation activity (Publication with Expression of Concern. See vol. 616, 2022), Journal of Colloid and Interface Science 587 (2021) 538–549. https://doi.org/10.1016/j.jcis.2020.11.011.

[27] D. Sun, B. Shen, S. Yang, X. Cheng, Q. Zhong, S. Abbas, Y. Dai, Y. Liu, C. Xu, C. Qi, H. He, S. Li, Nitrogen-doped CNTs enhance heterogeneous Fenton reaction for IOH removal by FeOCl: Role of NCNTs and mechanism, Separation and Purification Technology 326 (2023). https://doi.org/10.1016/j.seppur.2023.124763.
[28] M. Danish, X. Gu, S. Lu, A. Ahmad, M. Naqvi, U. Farooq, X. Zhang, X. Fu, Z. Miao, Y. Xue, Efficient transformation of trichloroethylene activated through sodium percarbonate using heterogeneous zeolite supported nano zero valent iron-copper bimetallic composite, Chemical Engineering Journal 308 (2017) 396–407. https://doi.org/10.1016/j.cej.2016.09.051.
[29] C. Lu, C. Jiao, Z. Wei, Zn-doped FeOCl nanosheets enable accelerated tetracycline degradation via simulated sunlight-responsive photo-Fenton catalysis, Materials Science in Semiconductor Processing 194 (2025). https://doi.org/10.1016/j.mssp.2025.109542.
[30] Q. Yu, M. Ding, Z. Wei, Z. Li, J. Zhao, H. Zhang, Photoelectrochemical studies of Sn doped FeOCl and photo-Fenton degradation of tetracycline, Journal of Solid State Chemistry 337 (2024). https://doi.org/10.1016/j.jssc.2024.124816.
[31] A. Li, Y. Wu, J. Zhou, X. Wang, Activation of peroxymonosulfate by Cu-doped iron oxychloride biochar for the degradation of tetracycline and disinfection of its resistant bacteria, Journal of Water Process Engineering 68 (2024). https://doi.org/10.1016/j.jwpe.2024.106318.
[32] Z. Wang, J. Wang, B. Xiong, F. Bai, S. Wang, Y. Wan, L. Zhang, P. Xie, M. Wiesner, Application of Cobalt/Peracetic Acid to Degrade Sulfamethoxazole at Neutral Condition: Efficiency and Mechanisms, Environmental Science & Technology 54(1) (2020) 464–475. https://doi.org/10.1021/acs.est.9b04528.
[33] Y. Ren, L. Lin, J. Ma, J. Yang, J. Feng, Z. Fan, Sulfate radicals induced from peroxymonosulfate by magnetic ferrospinel MFe2O4 (M = Co, Cu, Mn, and Zn) as heterogeneous catalysts in the water, Applied Catalysis B: Environmental 165 (2015) 572–578. https://doi.org/10.1016/j.apcatb.2014.10.051.
[34] Z. Yuan, Y. Ni, A.R.P.V. Heiningen, Kinetics of the peracetic acid decomposition: Part II: pH effect and alkaline hydrolysis, The Canadian Journal of Chemical Engineering (1997).
[35] J. Tomasi, M. Persico, Molecular Interactions in Solution: An Overview of Methods Based on Continuous Distributions of the Solvent, Cheminform 26(8) (1995).
[36] Y. Ji, Y. Fan, K. Liu, D. Kong, J. Lu, Thermo activated persulfate oxidation of antibiotic sulfamethoxazole and structurally related compounds, Water Research 87 (2015) 1–9. https://doi.org/10.1016/j.watres.2015.09.005.
[37] D. Barton, V. Le Gloahec, J. Smith, Study of a new reaction: Trapping of peroxyl radicals by TEMPO, Tetrahedron Letters 39(41) (1998) 7483–7486. https://doi.org/10.1016/s0040-4039(98)01628-1.
[38] D.F. Evans, M.W. Upton, Studies on singlet oxygen in aqueous solution. Part 3. The decomposition of peroxy-acids, Journal of the Chemical Society Dalton Transactions (6) (1985) 1151.
[39] S. Li, Y. Yang, H. Zheng, Y. Zheng, C.-S. He, B. Lai, J. Ma, J. Nan, Introduction of oxygen vacancy to manganese ferrite by Co substitution for enhanced peracetic acid activation and 1O2 dominated tetracycline hydrochloride degradation under microwave irradiation, Water Research 225 (2022). https://doi.org/10.1016/j.watres.2022.119176.
[40] M. Sun, I. Zucker, D. Davenport, X. Zhou, J. Qu, M. Elimelech, Reactive, Self-Cleaning Ultrafiltration Membrane Functionalized with Iron Oxychloride Nanocatalysts, Environmental Science & Technology 52(15) (2018) 8674–8683. https://doi.org/10.1021/acs.est.8b01916.
[41] C. Tan, X. Jian, Y. Dong, X. Lu, X. Liu, H. Xiang, X. Cui, J. Deng, H. Gao, Activation of

peroxymonosulfate by a novel EGCE@Fe3O4 nanocomposite: Free radical reactions and implication for the degradation of sulfadiazine, Chemical Engineering Journal 359 (2019) 594–603. https://doi.org/10.1016/j.cej.2018.11.178.
[42] Y. Yao, Y. Cai, F. Lu, F. Wei, X. Wang, S. Wang, Magnetic recoverable MnFe2O4 and MnFe2O4-graphene hybrid as heterogeneous catalysts of peroxymonosulfate activation for efficient degradation of aqueous organic pollutants, Journal of Hazardous Materials 270(apr.15) (2014) 61–70.
[43] M. Chen, H. Xu, Q. Wang, D. Li, D. Xia, Activation mechanism of sodium percarbonate by FeOCl under visible-light-enhanced catalytic oxidation, Chemical Physics Letters 706 (2018) 415–420. https://doi.org/10.1016/j.cplett.2018.06.004.
[44] J. Liu, R. Meng, J. Li, P. Jian, L. Wang, R. Jian, Achieving high-performance for catalytic epoxidation of styrene with uniform magnetically separable CoFe2O4 nanoparticles, Applied Catalysis B-Environmental 254 (2019) 214–222. https://doi.org/10.1016/j.apcatb.2019.04.083.
[45] C. Tan, T. Sheng, Q. Xu, T. Xu, K. Sun, L. Deng, W. Xu, Cobalt doped iron oxychloride as efficient heterogeneous Fenton catalyst for degradation of paracetamol and phenacetin, Chemosphere 263 (2021). https://doi.org/10.1016/j.chemosphere.2020.127989.
[46] X. Gao, W. Peng, G. Tang, Q. Guo, Y. Luo, Highly efficient and visible-light-driven BiOCl for photocatalytic degradation of carbamazepine, Journal of Alloys & Compounds 757 (2018) 455–465.
[47] J. Xu, L. Li, C. Guo, Y. Zhang, W. Meng, Photocatalytic degradation of carbamazepine by tailored BiPO4: Efficiency, intermediates and pathway, Applied Catalysis B Environmental 130-131 (2013) 285–292.
[48] Y.F. Rao, L. Qu, H. Yang, W. Chu, Degradation of carbamazepine by Fe(II)-activated persulfate process, JOURNAL OF HAZARDOUS MATERIALS 268(mar.15) (2014) 23–32.

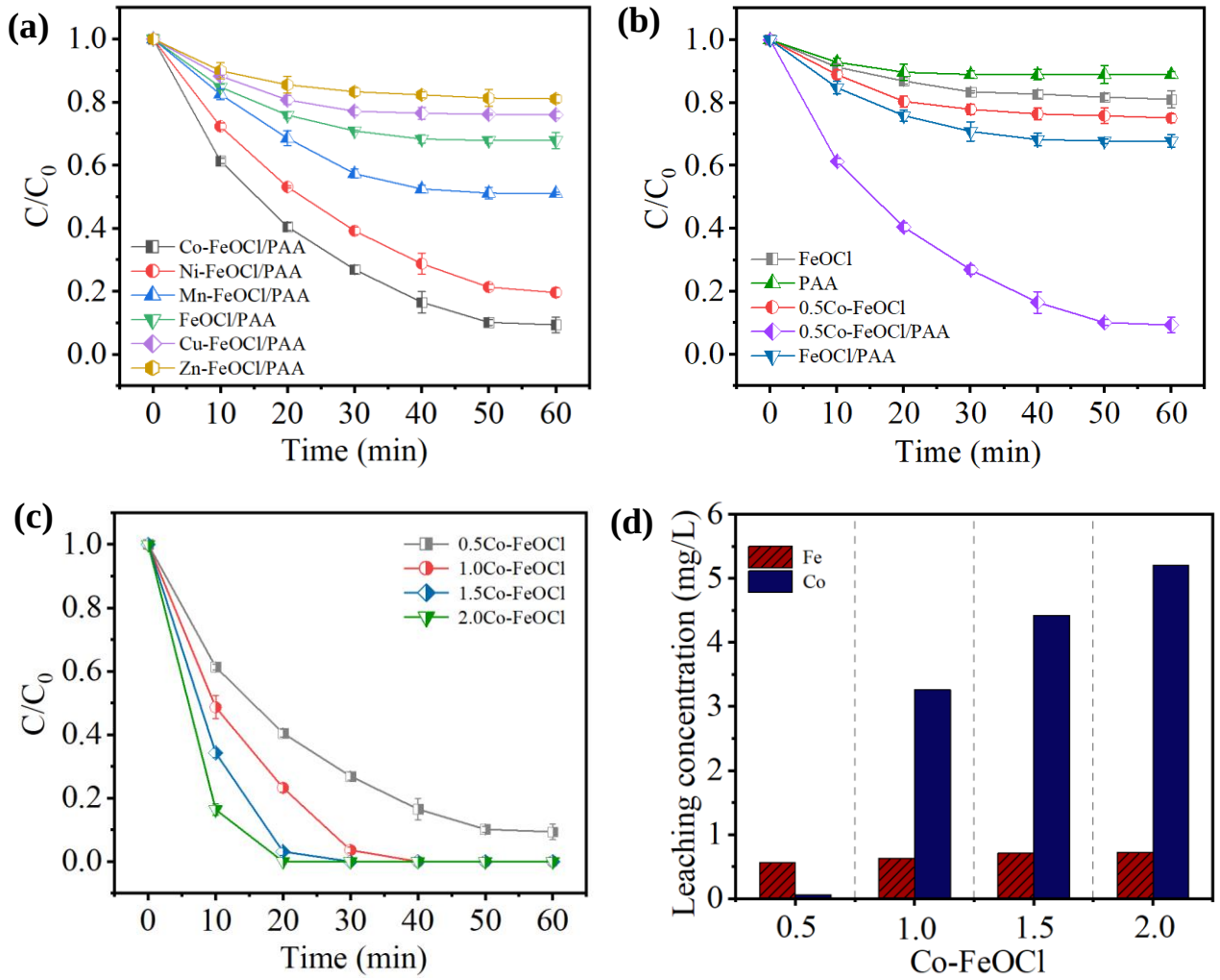


Figure 1. (a) CBZ removal by different metal-doped FeOCl (Co, Ni, Mn, Cu, Zn) in the presence of PAA; (b) CBZ removal by different systems; (c) the influence of Co doping level on the catalytic activity of Co-FeOCl and (d) corresponding Fe and Co ions leaching from different *x*Co-FeOCl. Reaction condition: [CBZ] = 10 μM, [Catalyst] = 0.1 g/L, [PAA] = 0.6 mM, and without solution pH adjustment.

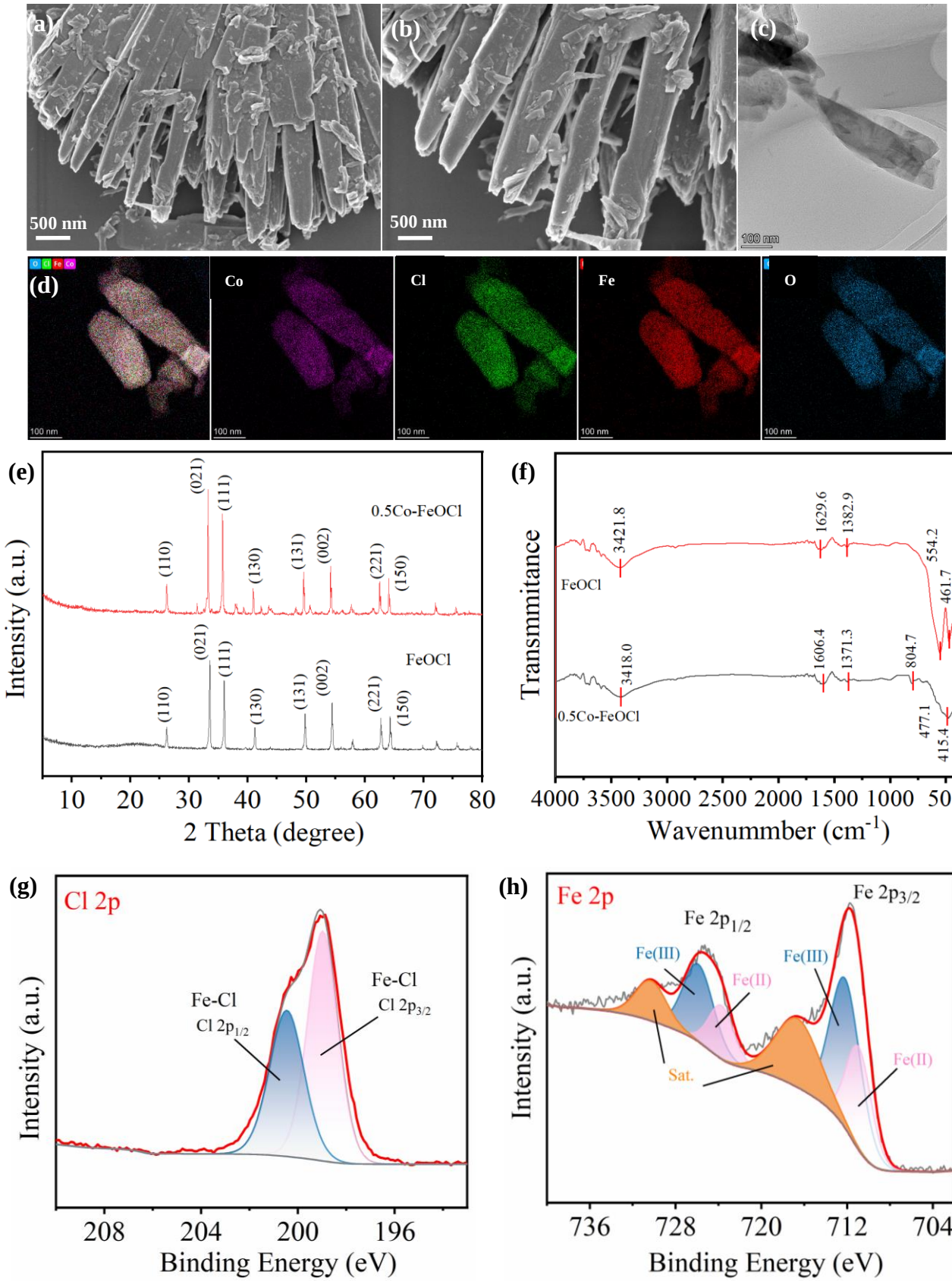


Figure 2. SEM images of (a) pristine FeOCl and (b) 0.5Co-FeOCl; (c) TEM image of 0.5Co-FeOCl; (d) EDS elemental mapping images of Co, Cl, Fe, and O in 0.5Co-FeOCl; (e) XRD patterns and (f) FTIR spectra of FeOCl and 0.5Co-FeOCl; XPS spectra of (g) Cl 2p and (h) Fe 2p in 0.5Co-FeOCl.

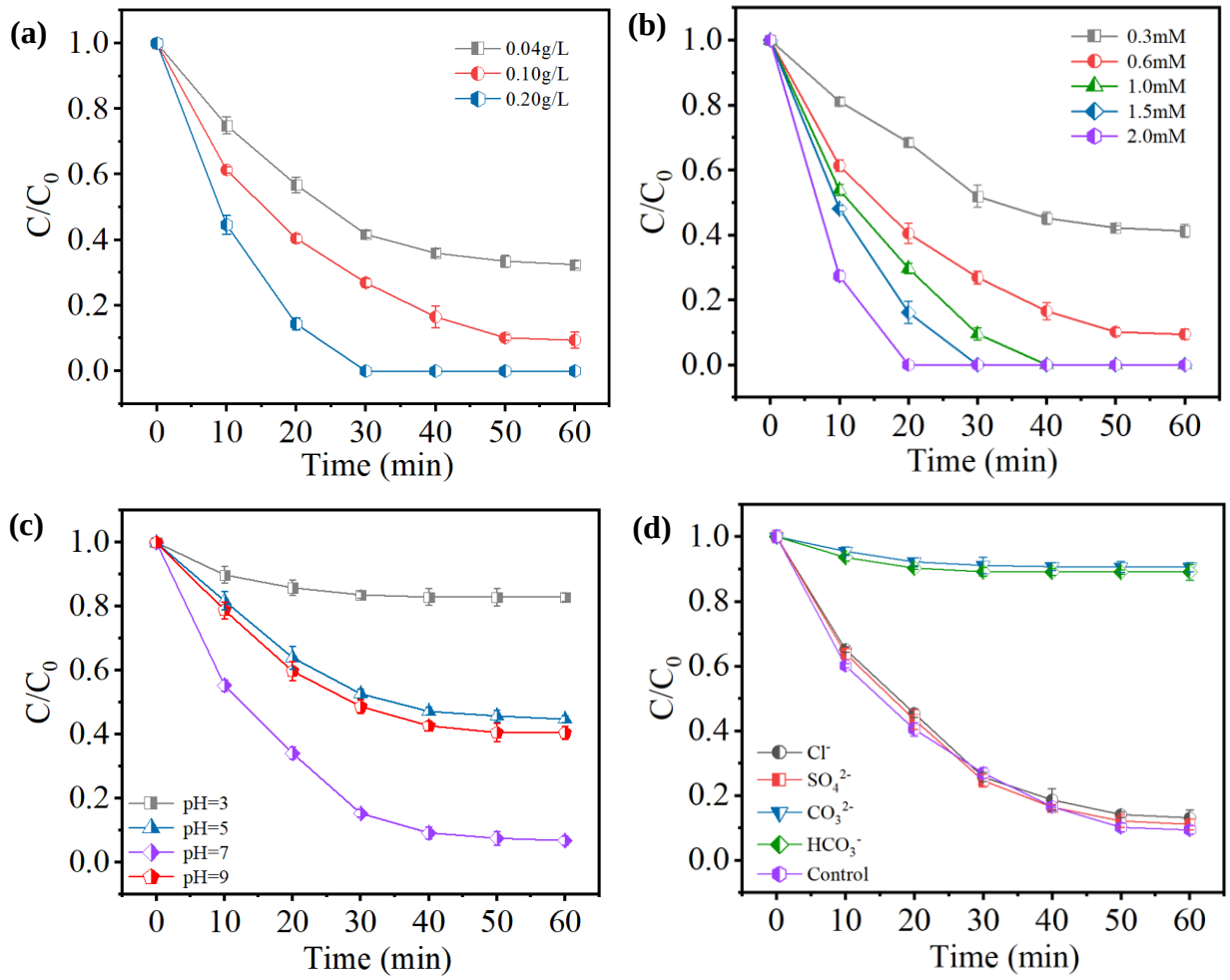


Figure 3. Effects of (a) 0.5Co-FeOCl dosage, (b) PAA concentration, (c) initial solution pH, and (d) common coexisting anions on CBZ removal in the 0.5Co-FeOCl/PAA system. Reaction conditions: unless otherwise noted, [CBZ] = 10 μM, [Catalyst] = 0.1 g/L, [PAA] = 0.6 mM, and without solution pH adjustment.

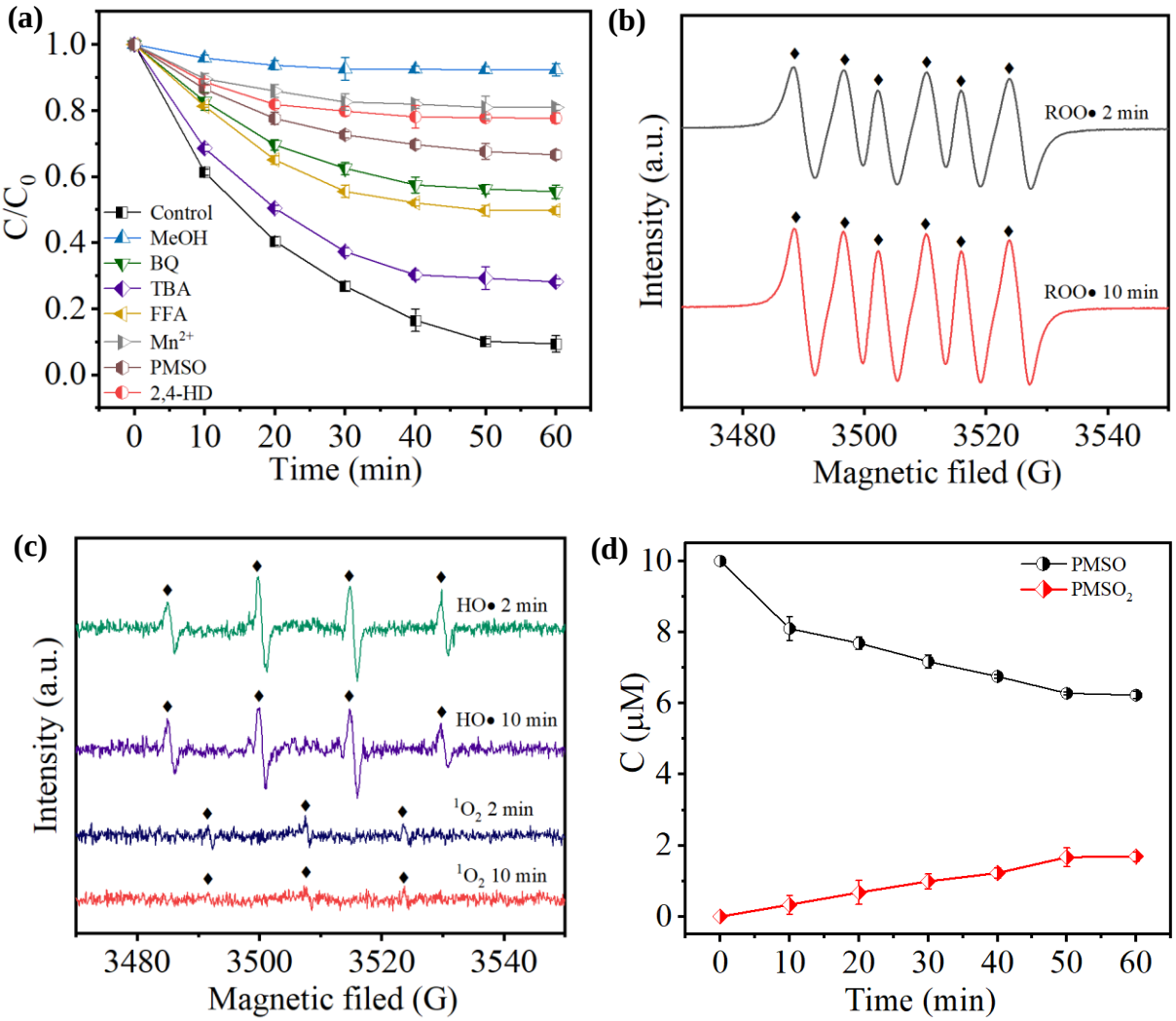


Figure 4. (a) The quenching tests using MeOH and TBA as scavengers ([CBZ] = 10 μM, [Catalyst] = 0.1 g/L, [PAA] = 0.6 mM, without pH adjustment, [MeOH] = 50 mM, [BQ] = 20 mM, [TBA] = 50 mM, [FFA] = 5 mM, [Mn^{2+}] = 10 mM, [PMSO] = 10 μM, and [2,4-HD] = 5 mM); EPR spectra of (b) DMPO-ROO•, (c) DMPO-•OH and TEMP-$^1O_2$ adducts; (d) PMSO consumption and $PMSO_2$ formation in the 0.5Co-FeOCl/PAA system.

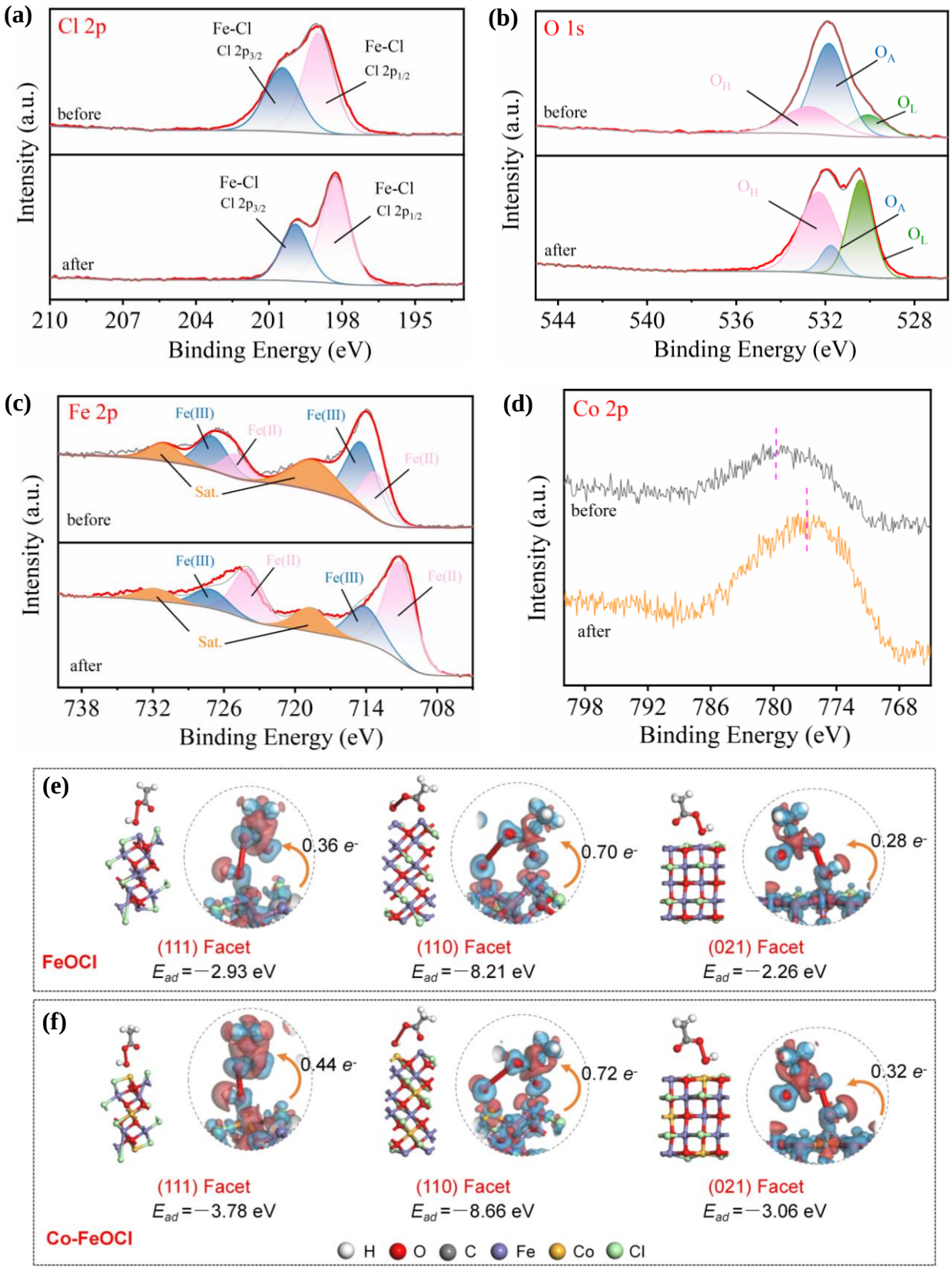


Figure 5. High-resolution XPS spectra of (a) Cl 2p, (b) O 1s, (c) Fe 2p, and (d) Co 2p in 0.5Co-FeOCl before and after the catalytic reaction. Optimized adsorption conformations and charge density difference of PAA on the (111), (110) and (021) facets of (e) FeOCl (f) and Co-FeOCl. Red and blue contours represent electron deletion and accumulation, respectively.

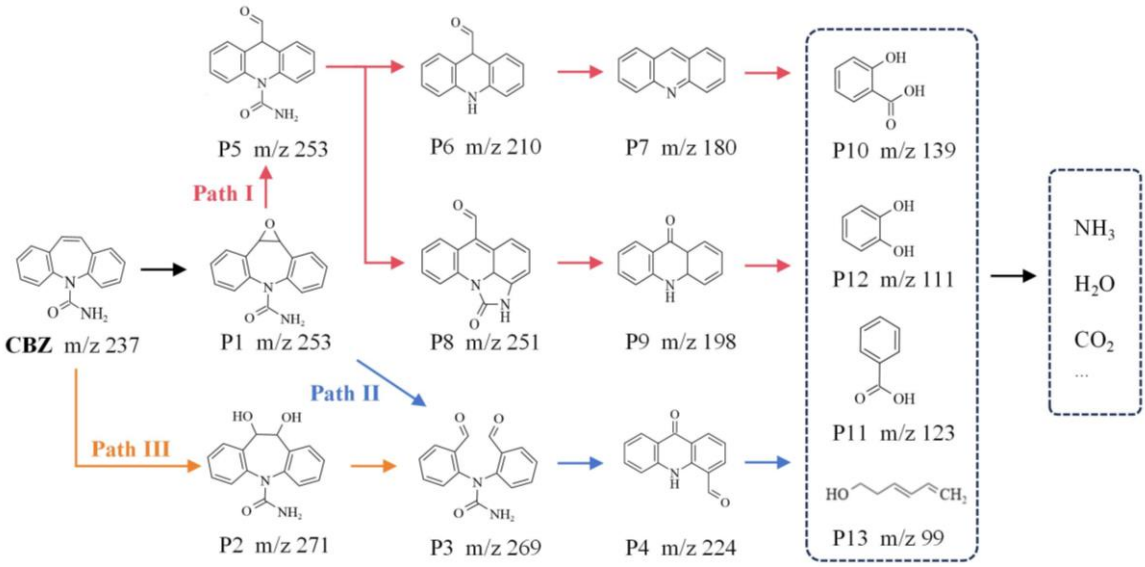


Figure 6. The possible degradation pathway of CBZ in the 0.5Co-FeOCl/PAA system.

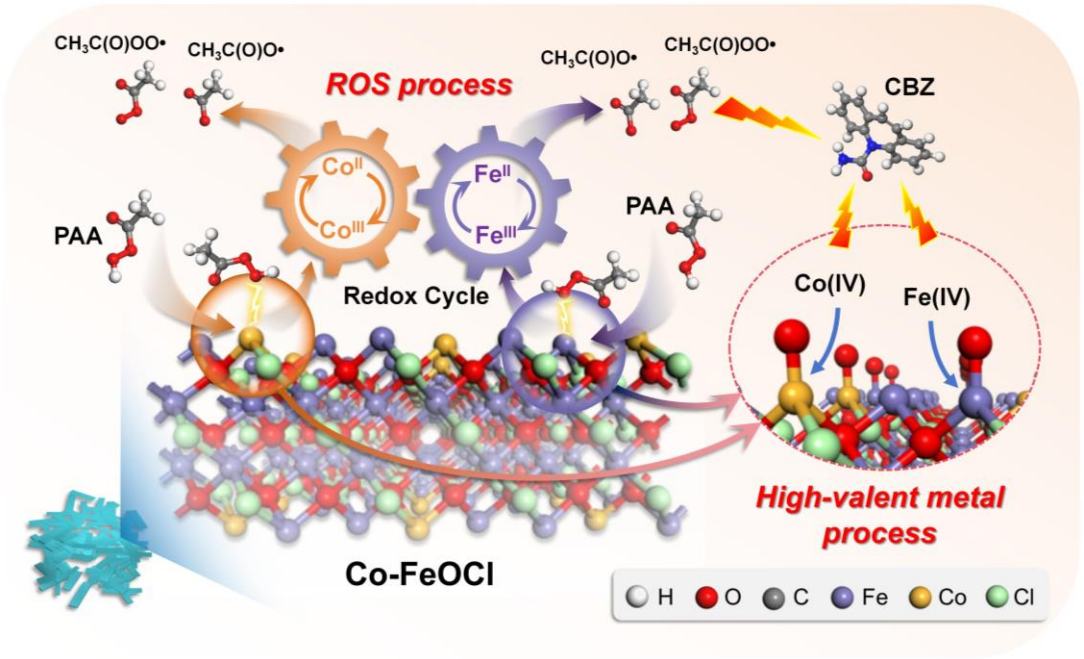


Figure 7. The proposed organic radicals and high-valent metals dominated mechanisms for CBZ degradation in the Co-FeOCl/PAA system.

Click here to access/download
Supplementary Material
Supplementary Material.doc